



Universiteit
Leiden
The Netherlands

Antisense oligonucleotide-mediated disruption of HTT caspase-6 cleavage site ameliorates the phenotype of YAC128 Huntington disease mice

Kuijper, E.C.; Overzier, M.; Suidgeest, E.; Dzyubachyk, O.; Maguin, C.; Pérot, J.B.; ... ; Roon-Mom, W. van

Citation

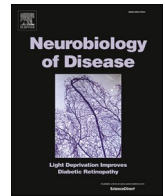
Kuijper, E. C., Overzier, M., Suidgeest, E., Dzyubachyk, O., Maguin, C., Pérot, J. B., ... Roon-Mom, W. van. (2023). Antisense oligonucleotide-mediated disruption of HTT caspase-6 cleavage site ameliorates the phenotype of YAC128 Huntington disease mice. *Neurobiology Of Disease*, 190. doi:10.1016/j.nbd.2023.106368

Version: Publisher's Version

License: [Creative Commons CC BY 4.0 license](#)

Downloaded from: <https://hdl.handle.net/1887/3720831>

Note: To cite this publication please use the final published version (if applicable).



Antisense oligonucleotide-mediated disruption of HTT caspase-6 cleavage site ameliorates the phenotype of YAC128 Huntington disease mice

Elsa C. Kuijper^{a,*}, Maurice Overzier^a, Ernst Suidgeest^b, Oleh Dzyubachyk^b, Cécile Maguin^c, Jean-Baptiste Pérot^{c,d}, Julien Flament^c, Yavuz Ariyurek^a, Hailiang Mei^e, Ronald A.M. Buijsen^a, Louise van der Weerd^{a,b}, Willeke van Roon-Mom^a

^a Department of Human Genetics, Leiden University Medical Center, the Netherlands

^b Department of Radiology, Leiden University Medical Center, the Netherlands

^c Université Paris-Saclay, Commissariat à l'Energie Atomique et aux Energies Alternatives, Centre National de la Recherche Scientifique, Molecular Imaging Research Center, Laboratoire des Maladies Neurodégénératives, France

^d Institut du Cerveau - Paris Brain Institute, Sorbonne Université, France

^e Department of Biomedical Data Sciences, Leiden University Medical Center, the Netherlands

ARTICLE INFO

Keywords:

Huntington disease
YAC128 mice
Antisense oligonucleotides
Caspase-6
RNA splicing
RNA sequence analysis
MRI

ABSTRACT

In Huntington disease, cellular toxicity is particularly caused by toxic protein fragments generated from the mutant huntingtin (HTT) protein. By modifying the HTT protein, we aim to reduce proteolytic cleavage and ameliorate the consequences of mutant HTT without lowering total HTT levels. To that end, we use an antisense oligonucleotide (AON) that targets HTT pre-mRNA and induces partial skipping of exon 12, which contains the critical caspase-6 cleavage site. Here, we show that AON-treatment can partially restore the phenotype of YAC128 mice, a mouse model expressing the full-length human HTT gene including 128 CAG-repeats. Wild-type and YAC128 mice were treated intracerebroventricularly with AON12.1, scrambled AON or vehicle starting at 6 months of age and followed up to 12 months of age, when MRI was performed and mice were sacrificed. AON12.1 treatment induced around 40% exon skip and protein modification. The phenotype on body weight and activity, but not rotarod, was restored by AON treatment. Genes differentially expressed in YAC128 striatum changed toward wild-type levels and striatal volume was preserved upon AON12.1 treatment. However, scrambled AON also showed a restorative effect on gene expression and appeared to generally increase brain volume.

1. Introduction

Huntington disease (HD) is a progressive neurodegenerative disorder caused by an expanded CAG repeat in exon 1 of the *HTT* gene and is inherited in an autosomal dominant manner. Normally, *HTT* contains 6 to 35 CAG repeats with each CAG triplet coding for a glutamine (Q) amino acid in the huntingtin (HTT) protein. In HD, the CAG repeat length exceeds 39 and repeat lengths of 36 to 39 are associated with reduced penetrance of the disease. Age of onset is inversely related with the CAG repeat length. The expanded polyglutamine repeat in the HTT

protein causes both loss of its normal function as well as a toxic gain of function. The mutation leads to neurodegeneration starting in the striatum, but extending to the whole brain eventually, causing motor, cognitive and psychiatric symptoms (Nopoulos, 2016; Tabrizi et al., 2022). Protein aggregates in brain are a pathological hallmark of the disease and nuclear inclusions are present in both neurons and glial cells (Rüb et al., 2016; Jansen et al., 2017).

As HTT is expressed in all cell types and involved in many cellular processes, pathologic mechanisms of HD are widespread. Deregulated pathways include transcriptional regulation, vesicle-mediated transport,

Abbreviations: aa586, amino acid position 586; aCSF, artificial cerebrospinal fluid; AON, antisense oligonucleotide; B6, C57BL/6; CSF, cerebrospinal fluid; FDR, false discovery rate; FL-hHTT, full-length human HTT; HD, Huntington disease; hHTT, human Huntingtin; HTT, huntingtin; ICV, intracerebroventricular; MRI, magnetic resonance imaging; N586-HTT, 586-N-terminal HTT; RARE, rapid acquisition with relaxation enhancement; SRR, super resolution reconstruction; TE, echo time; TR, repetition time; WT, wild-type.

* Corresponding author.

E-mail address: e.c.kuijper@lumc.nl (E.C. Kuijper).

<https://doi.org/10.1016/j.nbd.2023.106368>

Received 8 September 2023; Received in revised form 20 November 2023; Accepted 28 November 2023

Available online 29 November 2023

0969-9961/© 2023 The Authors. Published by Elsevier Inc. This is an open access article under the CC BY license (<http://creativecommons.org/licenses/by/4.0/>).

response to stress and autophagy (Tabrizi et al., 2022; Palaiogeorgou et al., 2023). Also, dysfunction of glial cells has been demonstrated leading to myelination defects, upregulated production of pro-inflammatory cytokines by microglia and diminished protection against excitotoxicity by astrocytes (Wilton and Stevens, 2020).

The main drivers of mutant HTT toxicity are thought to be its N-terminal fragments, produced either by alternative splicing or proteolytic cleavage (van der Bent et al., 2022). These N-terminal fragments contain the expanded polyglutamine tract that is encoded by exon 1 and tend to aggregate rapidly. Transgenic mouse models expressing N-terminal fragments of mutant HTT show a more progressive phenotype than transgenic mice expressing full-length mutant HTT (Farshim and Bates, 2018). *In vivo* HTT cleavage and nuclear accumulation of N-terminal fragments specifically have been demonstrated in *post mortem* HD brain and animal models prior to neurodegeneration (Wellington et al., 2002; Mende-Mueller et al., 2001; DiFiglia et al., 1997; Wang et al., 2008; Landles et al., 2010). Various proteases acting on HTT and their cleavage sites have been described (van der Bent et al., 2022). One of these is caspase-6, a protease that is mainly known for its role in apoptosis but is also involved in neurological processes such as axon pruning (Espinosa-Oliva et al., 2019). Cleavage of HTT by caspase-6 at amino acid position 586 (aa586) has been identified as crucial and rate-limiting event in the HTT cleavage cascade (Graham et al., 2006).

Since the YAC128 mouse model for HD expresses the full-length human HTT gene containing 128 CAG repeats, this model is suitable for studying the role of proteolytic cleavage (Slow et al., 2003). YAC128 mice expressing a mutant HTT version that is resistant to cleavage by caspase-6 at aa586 (C6R mice) do not show the neurodegeneration and behavioural phenotypes normally observed in YAC128 mice (Graham et al., 2006; Pouladi et al., 2009). In contrast, mice expressing mutant HTT resistant to cleavage by caspase-3 at aa513 and aa552 (C3R mice) displayed a similar phenotype as observed in YAC128 mice (Graham et al., 2006). Further confirming the toxicity of the caspase-6 cleavage fragment, expression of the 586-N-terminal HTT (N586-HTT) fragment containing a polyglutamine repeat of 82 in mice is sufficient to cause an HD-related phenotype (Tebbenkamp et al., 2011; Waldron-Roby et al., 2012). Also, it has been found that the N586-HTT fragment stabilizes pro-caspase-6 and promotes its activation, creating a feed-forward loop (Ehrnhoefer et al., 2019). Consistent with this, higher activity of caspase-6 has been observed in human and murine HD brain whereas expression was lower in C6R mice. Following cleavage at aa586, the N-terminal fragment is further cleaved into smaller toxic fragments and also the C-terminal fragment that is generated was reported to induce toxicity (Waldron-Roby et al., 2012; Wong et al., 2015; El-Daher et al., 2015).

Many therapeutic strategies have been proposed to reduce the toxicity of mutant HTT, of which the majority focuses on lowering HTT levels. Examples that have reached the clinical phase are tominersen, a gapmer antisense oligonucleotide (AON) targeting both wild-type and mutant HTT for degradation, and AMT-130, an adeno-associated viral vector expressing an HTT-targeting miRNA. However, questions remain about the safety viral delivery where dose correction is not possible (Tabrizi et al., 2022). Also, there is an ongoing discussion about lowering of HTT because of its important wild-type function, illustrated by embryonic lethality in *Htt* knockout mice and progressive neuropathological changes when HTT is eliminated in adult mice (Zeitlin et al., 1995; Dietrich et al., 2017). Nonetheless, a 75% reduction in mouse HTT seemed well tolerated in adult mice (Kordasiewicz Holly et al., 2012). Ideally, HTT lowering would be only targeting mutant HTT, but allele-specific strategies have not been successful so far (Kingwell, 2021). Hence, we aim to reduce toxicity of mutant HTT by targeting the generation of toxic proteolytic fragments while leaving HTT expression levels unchanged. Previously, reduction of caspase-6 has been proposed, but this may not be favourable as caspase-6 is involved in many processes and essential for proper brain function (Wong et al., 2015; Uribe et al., 2012). Moreover, other caspases have

been shown to be able to cleave HTT at aa586 as well when caspase-6 is ablated (Wong et al., 2015).

Therefore, we previously designed an HTT-targeting AON to inhibit the formation of toxic N-terminal fragments by targeting the rate-limiting caspase-6 cleavage site (Evers et al., 2014). This AON12.1 targets HTT exon 12 and induces a partial in-frame skip of exon 12, removing the region that encodes part of the caspase-6 cleavage motif (Fig. 1A). The resulting protein referred to as HTTA12 does not contain the caspase-6 cleavage motif and is resistant to cleavage at aa586 (Evers et al., 2014). Previously, we and others have shown the proof of concept of AON12.1 *in vitro* and *in vivo*, demonstrating successful exon skipping and formation of the HTTA12 protein (Evers et al., 2014; Casaca-Carreira et al., 2016; Kim et al., 2022). In addition, the HTTA12 protein has been shown to maintain the functional, biochemical and structural properties of canonical HTT and is able to support embryonic development (Kim et al., 2022).

In this study, we sought to determine the therapeutic effect of AON12.1 on the behavioural and molecular phenotype in YAC128 mice. YAC128 mice were originally generated in a FVB/N background but because of their susceptibility to epileptic seizures and visual impairment, we chose to use the YAC128 line on C57BL/6 (B6) background (Stéphane et al., 2016). The YAC128/B6 model presents early behavioural deficits and striatal volume reduction from 12 months of age. As observed in other models expressing full-length HTT, body weight is increased in YAC128 mice (Slow et al., 2003; Teo et al., 2016; Brooks et al., 2012; Van Raamsdonk et al., 2007). Here, we showed that intracerebroventricular (ICV) administration of AON12.1 led to a partial rescue of the behavioural phenotype observed in YAC128 mice and could ameliorate striatal volume reduction and striatal gene expression changes.

2. Materials and methods

2.1. Animals

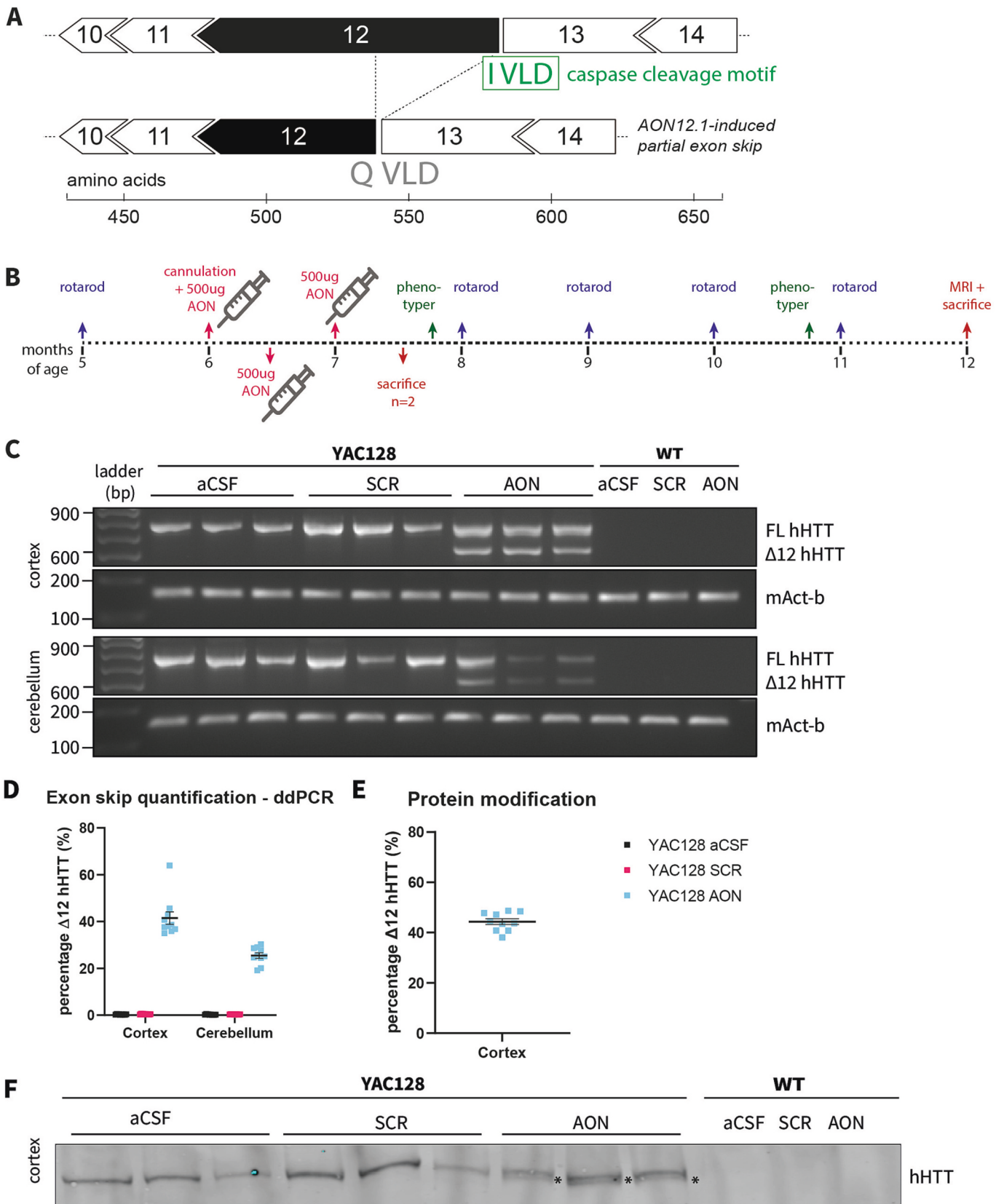
This study was performed in transgenic YAC128 mice maintained on a C57BL/6 (B6) background, originally obtained from the Jackson Laboratory (#027432), and wild-type litter mates. Only male mice were included. All animal experiments were performed in accordance with European Communities Council Directive 2010/63/EU and were approved by the Leiden University animal ethical committee (AVD1160020171069). Mice were housed in individually ventilated cages with *ad libitum* food and water access and a 12 h light/dark cycle. After placement of the cannula, mice were housed individually to prevent damage to the cannulas. Genotyping was done on ear clip tissue material, applying a Phire animal tissue direct PCR kit (ThermoFisher Scientific) using primers targeting human *Htt* exon 1 5' of the CAG repeat and the mouse Interleukin-2 gene (Table 1). The multiplex PCR was performed according to manufacturer's instructions and consisted of 36 cycles of 5 s of denaturation at 98 °C, 5 s of annealing at 66.5 °C and 20 s of extension at 72 °C. Genotyping was repeated after sacrifice for genotype confirmation.

2.2. Antisense oligonucleotides (AONs)

2'-O-methoxyethyl-modified phosphorothioate AON12.1 (GTCCCATCATTGAGGTCCAT) and scrambled AON (TCGTGCTACCCTCGAAATCT) were synthesized by ProQR using standard solid phase phosphoramidite chemistry according to previously published protocols (Capaldi and Scozzari, 2007). AONs were purified using AEX-HPLC and subsequently dissolved in artificial CSF (aCSF, Tocris) with end concentration of 50 µg/µL.

2.3. AON injections

Starting at approximately 6 months of age, treatment was



(caption on next page)

Fig. 1. Treatment scheme and validation of AON-mediated exon skip.

A) The caspase-6 cleavage motif is encoded by the 3' end of exon 12 and 5' part of exon 13. The AON-induced in-frame exclusion of the 3' part of exon 12 leads to disruption of the caspase-6 cleavage motif. B) Baseline measurements were performed at 5 months of age. Three injections were given between 6 and 7 months. Monthly behavioural testing was done up to 12 months of age, when an MRI scan was acquired and mice were sacrificed. C) Representative results of RT-PCR for Htt exon 9 to 14, showing skipped hHTT RNA ($\Delta 12$ hHTT) in addition to unskipped hHTT (FL hHTT) specifically in the AON-treated YAC128 mice. As expected, no hHTT is expressed in wild-type (WT) mice. D) The percentage of $\Delta 12$ hHTT RNA from total hHTT RNA was determined using ddPCR, showing about 40% skip in cortex and 25% in cerebellum (average of 2 technical replicates). E) Western blot was used to detect both $\Delta 12$ hHTT and FL hHTT protein and calculate the levels of hHTT $\Delta 12$ as percentage of total hHTT protein, which showed about 44% protein modification. F) Representative results of hHTT detection with 1C2 antibody on western blot demonstrating the appearance of the $\Delta 12$ hHTT protein (indicated with *), which is 5 kDa smaller than full-length (FL) hHTT. The same mice are shown as in C. Mean + SEM shown. D –F: N = 10 per group.

Table 1

Primers and probes used for genotyping and exon skip quantification.

Primer target	Sequence	Application
Htt_oIMR1594	CCGCTCAGGTTCTGCTTTTA	Genotyping – human HTT
Htt_oIMR1596	TGGAAGGACTTGAGGGACTC	Genotyping – human HTT
Htt_oIMR7338	CTAGGCCACAGAATTGAAAGATCT	Genotyping – mouse IL2
Htt_oIMR7339	GTAGGTGAAAATTCTAGCATCATCC	Genotyping – mouse IL2
hHTT _{exon9_14-fw}	GAGCTTCTGCAAACCTGAC	PCR – human HTT
hHTT _{exon9_14-rev}	CTGCCTGCAGTACTCATGT	PCR – human HTT
mActbQex2fw	GGCTGTATTCCCTCCATCG	PCR – mouse β -actin
mActbQex3rev	CCAGTTGGTAACAATGCCATGT	PCR – mouse β -actin
$\Delta 12$ hHTT probe	/56-FAM/CCAGCCAGGTGTTAGACGG/3BHQ_1/	ddPCR – $\Delta 12$ hHTT detection
$\Delta 12$ hHTT fw primer	GCCACTGATGGGGATGAGGAGGA	ddPCR – $\Delta 12$ hHTT detection
$\Delta 12$ hHTT rev primer	ATGTGCCTGTTGAAGGCCATGG	ddPCR – $\Delta 12$ hHTT detection
FL hHTT probe	/5HEX/CCCTTCAGACAGTTCTGAAATTGTGTT/3BHQ_1/	ddPCR – FL hHTT detection
FL hHTT fw primer	GACAGCTCCAGACCACCACC	ddPCR – FL hHTT detection
FL hHTT rev primer	AGGCTGCCTGCAGTACTCAT	ddPCR – FL hHTT detection

administered intracerebroventricularly (ICV) as described before (Metz et al., 2022). In short, mice were anesthetized using isoflurane and placed in a stereotactic device to enable placement of non-metallic cannulas in the lateral ventricle. 500 μ g AON12.1 or 500 μ g scrambled AON diluted in 10 μ L aCSF or 10 μ L aCSF alone was injected and the cannula was fixed to the skull using Diafil dental cement (Diadent). The second and third injection were performed 2 and 4 weeks after surgery under isoflurane anesthesia.

2.4. Behavioural experiments

Motor behaviour was assessed using the rotarod (Ugo Basile). A baseline measurement was performed at 5 months of age. From 8 months of age, one month after the last injection, up to 11 months of age the rotarod was performed monthly. The rotarod consisted of three sessions on one day with intervals of 1.5–2 h. The rod accelerated from 5 to 40 rpm in 5 min. Mice were allowed to stay on the rod for a maximum of 5 min and the latency to fall was recorded. The maximum latency to fall over the three sessions was calculated. For the timepoints after treatment, it was also registered if and at what time mice stopped running and clung to the rod instead, turning around without falling off

(‘latency to turn around’).

To measure home cage activity and anxiety behaviour, mice were placed in a phenotyper cage (Noldus) for 3 subsequent days and nights at 8 and 11 months of age. The phenotyper cage contained a shelter (adjusted in height because of the cannula on the head) with nesting material. The movement of the mice was continuously tracked by EthoVision XT 13 software for calculation of the distance moved and time spent in the different areas of the cage (Fig. S1). As tracking was lost sometimes when mice were in their shelter, we calculated the total shelter time as sum of the tracked time in their shelter (hidden zone) and the time the mice were not detected. To assess anxiety, we used the light spot test adapted from Aarts et al. (Aarts et al., 2015). During the third dark period, the light incorporated in the phenotyper cage topunit above the food area was put on from 20.15 to 21.15 h as an anxiety stimulus. Outcome measures were generated per hour for day/night 1 and day/night 2 to investigate spontaneous behaviour. To assess the response to the light stimulus during night 3, outcome measures were retrieved per 15 min from one 19.00 to 23.00 h. Main outcome measures for statistical analysis were total distance moved and time spent in the shelter during day/night 2. For exploratory analysis, the (relative) time spent in the food area and anxiety outcomes were assessed.

At 12 months of age, an MRI scan was made after which the mice were directly sacrificed by CO₂ inhalation. Body weight was measured before surgery and subsequent injections, before every phenotyper cage and rotarod experiment and before MRI.

2.5. MRI

MRI was conducted on a 7 Tesla Bruker PharmaScan® (Bruker BioSpin) equipped with an 1H 089/072 (T20117V3) coil for transmit, 1H M. Head 3 \times 1 (T20187V3) coil for receive and ParaVision version 360.1.1 (Bruker BioSpin). For practical reasons, only aCSF-treated wild-type mice and all YAC128 mice were included. Scanning was performed under general anesthesia using isoflurane (4% for induction, 1.5% for maintenance) in a 3:1 mixture of air and oxygen (total flow 0.6 L/min). During the scan, mice were positioned on a heated water bed with constant body temperature monitoring (Medres) and respiratory function was assessed with a pressure-sensitive pad (Small Animal Instruments Inc.). For volumetric analysis, T2-weighted images were acquired using a 2D RARE sequence in both coronal and axial planes (repetition time (TR) 2632.24 ms; echo time (TE) 9 ms, effective TE 36 ms; field of view 20 \times 20 mm²; slice thickness 0.5 mm; in-plane resolution 80 \times 80 μ m²; 19 slices, RARE factor 10; 8 averages).

Super resolution reconstruction (SRR) was performed on the two acquired anisotropic volumes using the approach described (Dzyubachyk et al., 2015) to improve the through-slice resolution. For this, the transversal volume was initially mapped to the corresponding coronal one, after which misalignment (displacement) between the two volumes was estimated using the gradient-correlation-based method (Dzyubachyk et al., 2015). Finally, SRR was performed with the through-slice resolution improvement factor of 2 and the initial and final regularization factors equal to $\lambda_i = 5$ and $\lambda_f = 0.1$, respectively. Subsequently, images were co-registered and automatically segmented using an in-house python library (Samba-MRI (Celestine et al., 2020)) as described before (Pérot et al., 2022). First, anatomical images were co-

registered to generate an average of all anatomical images, called the study template. This template was segmented using an atlas composed by 34 regions derived from the Allen mouse brain atlas (Table S1) (Lein et al., 2007). Then, transformations to match the atlas to the study template and to match the study template to all high-resolution anatomical images were calculated. Finally, transformations were computed with AFNI (Cox, 1996) to project the atlas onto the images. Additionally, to deal with heavy skull deformations, a brain mask obtained with the RATS toolbox (Oguz et al., 2014; Yin et al., 2010) was used to cut out parts of the atlas projections that would go over the edges. Outputs of the Samba-MRI pipeline are the volume of each of the 34 structures. As segmentation of hindbrain structures showed disturbances, we did not assess the arbor vita of cerebellum, cerebellar cortex, colliculus, medial lemniscus, medial longitudinal fasciculus, medulla, midbrain, periaqueductal gray and pons. The remaining regions were referred to as 'cerebrum'. We selected and assessed the volume of 9 regions that are relevant for HD: striatum, pallidum, thalamus, total cortex, fimbria, corpus callosum, hippocampus, lateral ventricle and cerebrum.

2.6. Tissue isolation

Upon sacrifice, the brain was isolated. The right hemisphere was fixed in 4% PFA for about 24 h at room temperature (RT), then put in 30%-sucrose/0.02% sodium azide solution at 4 °C for at least 24 h until being frozen in isopentane placed on dry ice and stored at -80 °C. Brainstem, cerebellum, cortex, hippocampus, midbrain and striatum were dissected from the left hemisphere, snap frozen using liquid nitrogen and stored at -80 °C.

2.7. Cryosection and immunohistochemistry

Using a Leica CM3050 S cryostat, coronal sections of 25 µm thickness were collected from PFA-fixed hemispheres as free-floating sections in PBS/0.02% sodium azide and stored at 4 °C until staining. For staining of DARPP32, sections were washed in PBS+ (1×PBS + 0.1% Triton) and primary antibody (Ab40801, Abcam, 1:2000) was incubated o/n at 4 °C in immune buffer (0.1% Triton +1% normal goat serum +0.04% merthiolate in 1× PBS). After washing in PBS+, secondary antibody (anti-rabbit Alexa594 A11012, Invitrogen, 1:500) was incubated for 2 h at RT in the dark. Subsequently, sections were washed with PBS and incubated with DAPI (1:1000, D9542, Sigma Aldrich) for 15 min at RT. Sections were washed with PBS, put on SuperFrost Plus slides (Thermo Scientific) and mounted with ProLong Diamond Antifade Mountant (ThermoFisher). All wash and incubation steps took place while shaking. The Keyence BZ-X810 was used for imaging the striatum at 4× magnification. Analysis was performed in ImageJ. Based on the DAPI staining, the striatum was selected as region of interest (ROI) and here the mean intensity of DARPP32 staining was measured.

2.8. RNA isolation, RT-PCR and ddPCR

RNA was isolated from about 30 mg of cortex, cerebellum and striatum using the PureLink RNA mini kit (Thermo Fisher Scientific) including a 15 min DNase treatment step. Tissue was homogenized in 700 µL lysis buffer in MagNA Lyser Green beads tubes (Roche) with bullet blender Storm 24 (Next Advance) for 2–3 min at setting 8. RNA was eluted in 30 µL nuclease-free water and concentrations were measured using the Nanodrop (Thermo Fisher Scientific).

For cortex and cerebellum, cDNA was synthesized from 500 ng RNA with the Transcriptor First Strand cDNA synthesis kit (Roche) using random hexamer primers. Exon skip efficiency was assessed using PCR and ddPCR. For the former, cDNA was diluted 20× and using Faststart Taq DNA Polymerase (Roche) a human HTT (hHTT) fragment and mouse β-actin fragment were amplified with primers listed in Table 1 using the following PCR program: initiation 4 min 95 °C; 36 cycles of 30

s 95 °C denaturation, 30 s 59 °C annealing, 1 min 72 °C extension; 7 min 72 °C final elongation. PCR products were run on a 2% agarose gel containing 0.0033% ethidium bromide and visualized with the OptiGo-750 (Isogen Life Science).

To quantify the exon skip, a probe-based ddPCR assay was designed for both specific amplification of the unskipped hHTT RNA and of the skipped hHTT RNA (see primers and probes in Table 1) using the ddPCR Supermix for probes (Bio-Rad). cDNA input was equivalent to 12.5 ng RNA per reaction. Droplets were generated with the Automated Droplet Generator (Bio-Rad). The PCR reaction consisted of 10 min 95 °C initiation; 40 cycles of 30 s 94 °C, 1 min 58 °C; final 10 min 98 °C, all with a ramp rate of 2 °C/s. After the PCR reaction, droplets were counted with the QX200 Droplet reader (Bio-Rad) and analysis was done with the QuantaSoft Analysis Pro software (Bio-Rad) setting a manual threshold of 1500 for both channels. Exon skip efficiency was calculated by dividing the concentration of skipped hHTT RNA by the sum of concentrations for skipped and unskipped hHTT RNA. For each sample, the average of two ddPCR runs was calculated.

2.9. RNA sequencing

RNA from striatum was sequenced using NovaSeq for aCSF-treated wild-type mice and all YAC128 mice. For each group, 8 samples were selected based on the following criteria: no unrelated health issues observed, having received 3 injections and highest RNA concentration. RNA quality was assessed using FEMTO Pulse, showing a RIN value >8.0 for all samples. Full-length cDNA generation, Illumina library preparation and Illumina paired-end sequencing was performed as described in Kenkhuis et al. (Kenkhuis et al., 2022). In short, full-length cDNA was generated using the mcSCR-seq method with modifications (Bagnoli et al., 2018). Samples were uniquely barcoded using the well barcode, and the handle for Read 2 sequence primer allowed further barcoding of a pool of samples by adding the i7 Illumina barcode and the p7 sequence. The pooled cDNA libraries were generated using the 2× Kapa HiFi HotStart mix (Roche). The Illumina library prep was performed using the Kapa Hyper Plus kit (Roche) with fragmentation, end-repair, A-tailing, and double SPRI purification. Custom indexed adapter barcodes were used to barcode the pool of samples using the i5 Illumina barcode and introduce the p5 sequence to complete the Illumina library. The ligated products were purified using Ampure beads, and PCR with Kapa Mastermix (Roche) and p5 and p7 primers was performed for enrichment. After double SPRI size selection, the Illumina library was quantified and checked for size distribution. Illumina paired-end sequencing was performed on a NovaSeq 6000 using the manufacturer's instructions. To facilitate pipeline analysis, the UMI from the Read 2 fastq file was added to the beginning of the same read ID in the Read 1 fastq file, resulting in a modified Read 1 fastq file starting with the UMI followed by the cDNA sequence, which was used in the RNA-seq pipeline.

RNAseq reads were processed using the opensource BIODL RNAseq pipeline v5.0.0 (<https://zenodo.org/record/5109461#.Ya2yLFPMJhE>) developed at the LUMC. This pipeline performs FASTQ preprocessing (including quality control, quality trimming, and adapter clipping), alignment, read quantification, and optionally transcript assembly. FastQC was used for checking raw read QC. Adapter clipping was performed using Cutadapt (v2.10) with the default settings. RNAseq reads' alignment was performed using STAR (v2.7.5a) on a customized mouse reference genome where GRCm39 mouse reference genome is combined with the *Homo sapiens* huntingtin (HTT), transcript variant 1 (NM_001388492). The gene read quantification was performed using HTSeq-count (v0.12.4) with setting "--stranded = yes". The gene annotation used for quantification was Ensembl version 106 with an added entry for the HTT transcript (NM_001388492).

Differential gene expression analysis was performed in R (v4.0.2) using DESeq2 (v1.30.1) on separate data sets containing the samples of two groups to be compared, selecting genes with >5 counts per million

for at least 7 samples. Differential expression was performed using the DESeq-function with default settings and results were extracted with disabled independent filtering. Genes with an adjusted *P*-value (Benjamini-Hochberg) of <0.1 were considered significantly differentially expressed. Official gene symbols were assigned to ENSEMBL identifiers using the getBM function of biomaRt package (v 2.46.3). Vst-transformed data was visualized using heatmap (v1.0.12) applying scaling per row.

For pathway assessment, overrepresentation analysis was performed using GeneTrail 3.2 (Gerstner et al., 2020) applying Benjamini-Yekutieli FDR *P*-value adjustment and a significance level of 0.05.

2.10. Protein isolation

For protein isolation, about 30 mg of cortex and cerebellum was homogenized in RIPA buffer (50 mM Tris-HCl pH 8.0, 150 mM NaCl, 1% IGEPAL CA-630, 0.5% DOC, 0.1% SDS) including protease inhibitors (1 tablet per 10 mL, Roche) using the bullet blender. Subsequently, supernatant was incubated at 4 °C for 30 min and centrifuged at 15,000 ×g at 4 °C for 10 min. Protein concentration of the supernatant was determined with a BCA assay (Thermo Fisher Scientific). Glycerol was added to a final concentration of 5% and protein lysates were snap frozen and stored at –20 °C until further analysis.

2.11. Western blot

For detection of HTT, 40 µg protein isolated from cortex was loaded on 3–8% Criterion XT tris-acetate gel (Bio-Rad) under reducing conditions next to the Spectra Multicolor High Range protein ladder (Thermo Scientific). To detect HTT protein modification, gels were run for 30 min at 80 V, 2 h at 100 V, then put on ice and run for 4 h at 120 V. For detection of N-terminal fragments, gels were run for 20 min at 80 V and then 2 h at 100 V. For detection of Car2 and IL33, respectively 15 and 45 µg was run on 10% Bis-Tris gel (Bolt). Semi-dry transfer to nitrocellulose (Bio-Rad) was performed using the standard protocol on the TransBlot Turbo system (Bio-Rad). After blocking with 5% milk/TBS for 1 h at RT, primary antibodies (Table 2) were diluted in 5% milk/TBS(T) and incubated o/n at 4 °C. Membranes were washed with TBST and incubated with secondary antibodies (Table 2) diluted in 5% milk/TBS(T) for 1 h at RT. After washing with TBST, membranes were scanned on the Odyssey imaging system (LI-COR Biosciences). IL33 was detected after incubating with Pierce ECL substrate using the Amersham Imager 680 (GE). Signal was quantified using Image Studio Lite (LI-COR

Table 2
Antibodies used for western blot.

Primary antibodies				
Protein	Catalog number	Supplier	Dilution	Species
Huntingtin (expanded polyglutamine tract)	5TF1-1C2	Euromedex	1:2000	Mouse
Vinculin	700,062	Invitrogen	1:1000	Rabbit
Car2	NB600–919-100µg	Novus biologicals	1:1000	Rabbit
IL33	AF3626	R&D systems	1:500	Goat
β-actin	ab6276	Abcam	1:5000	Mouse
Secondary antibodies				
Antibody	Catalog number	Supplier	Dilution	Species
Anti-mouse IRDye680	926–68,070	Li-Cor	1:5000/ 1:10,000	Goat
Anti-rabbit IRDye800	926–32,211	Li-Cor	1:5000/ 1:10,000	Goat
Anti-goat HRP	sc-2033	SantaCruz	1:20,000	Donkey

Biosciences). Protein modification was quantified as the percentage of HTTΔ12 signal of the total signal of HTTΔ12 and FL-HTT (Fig. S2). For other quantifications, signal of the protein of interest was normalized to the signal of the housekeeping protein (vinculin or β-actin). For Car2 and IL33 and their housekeeping protein, signal was first calculated relative to the average level in aCSF-treated wild-type mice before normalization as absolute signal levels varied per blot.

2.12. Statistical analysis

Statistical analysis was done in GraphPad Prism 9.0.1. For the longitudinal outcomes, fixed effects ‘time’ and ‘group’ and their interaction were assessed using a mixed-effects model. The differences among the groups at individual time points and in molecular assays and MRI were analysed using the Kruskal-Wallis test with Dunn's multiple testing correction as not all data were normally distributed.

3. Results

3.1. Intracerebroventricular AON administration induced Htt exon skip in brain

YAC128 and wild-type mice were treated with vehicle (aCSF), a scrambled AON (Scr) or AON12.1 (AON) starting at 6 months of age and followed up to 12 months of age (Fig. 1B). Two mice were sacrificed two weeks after the last injection to confirm presence of the exon skip (Fig. S3). During genotyping after sacrifice, one mouse that was originally included as transgenic turned out to be wild-type. A total of 9 mice were excluded from the study due to experimental considerations (mixed identity of mice, incomplete number of drug administrations or premature death). In total, 9 or 10 mice per group were included for the analysis (Table S2).

To confirm successful treatment, the partial skip of exon 12 was evaluated on RNA level with RT-PCR. All YAC128 mice treated with AON12.1 showed an additional PCR fragment representing the skipped RNA both in cortex and cerebellum (Fig. 1C, Fig. S4). To quantify the partial exon skip, we used a ddPCR assay with probes specific for the skipped human HTT (Δ12 hHTT) or unskipped full length human HTT (FL-hHTT)(Fig. S5). In cortex, around 40% of total hHTT was skipped 5 months after AON treatment and 25% skip was detected in cerebellum (Fig. 1D).

Next, protein modification was assessed in the cortex using western blotting (Fig. S6). In addition to the full length hHTT protein band, AON-treated YAC128 mice showed a second band approximately 5 kDa smaller than full length hHTT representing the modified protein. On average, 44% of total hHTT protein was modified (Fig. 1E-F). Separate blots were run for detection of total hHTT and its N-terminal fragments. Total hHTT levels were not changed, which is an important aspect of our exon skipping approach (Fig. S7A–B). The levels of N-terminal fragments depicted a tendency to be decreased in AON-treated YAC128 mice, but this was not significant (Fig. S7A,C).

3.2. AON treatment rescued the YAC128 phenotype on weight and activity but not on the rotarod

To investigate the effect of AON treatment on the phenotype of YAC128 mice, their weight, motor performance and activity levels were assessed. Baseline measurements were performed at 5 months of age. Starting one month after the last injection, at 8 months of age, up to 11 months of age the rotarod was performed monthly and body weight was measured (Fig. 1B).

The average body weight was significantly higher in YAC128 mice than in wild-type mice at 5 months of age (Fig. 2A). The impact of intracerebroventricular cannulation at 6 months of age was visible on body weight, showing a decrease in body weight in all groups that reversed again when treatment was completed. Body weight in aCSF-

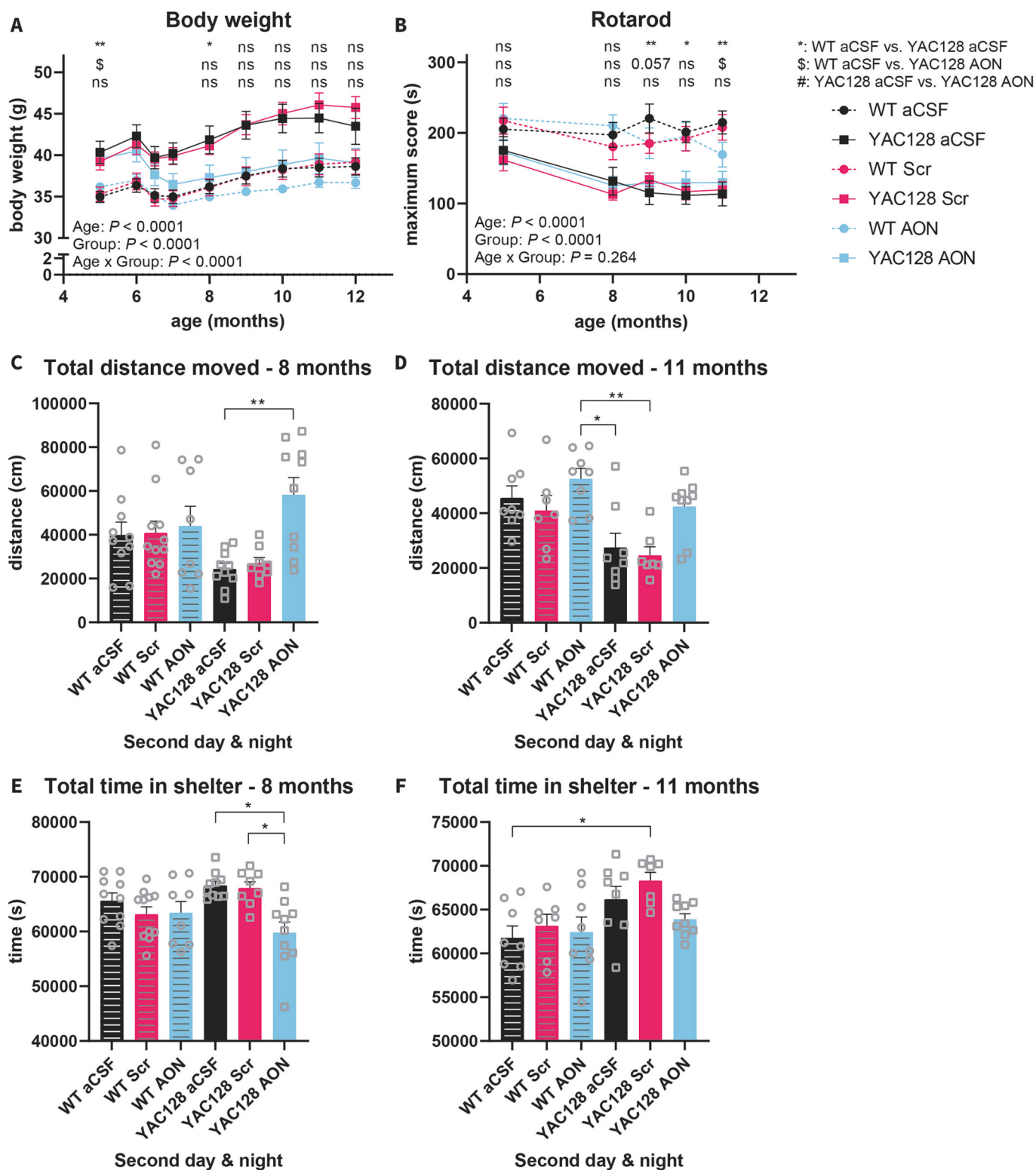


Fig. 2. AON treatment led to partial rescue of the YAC128 phenotype on weight and behaviour.

A) Body weight was assessed longitudinally throughout the study. At baseline, YAC128 mice showed a higher weight compared to wild-type mice. AON12.1 (AON) treatment restored the body weight of YAC128 mice to wild-type levels. B) On the rotarod, YAC128 mice showed a shorter latency to fall (maximum score from three trials) than wild-type mice. AON12.1 treatment did not restore this phenotype. Both at 8 months (C,D) as at 11 months of age (E,F), the total distance moved during the second day in the phenotyper cage appeared to be lower for YAC128 mice treated with aCSF and scrambled AON (Scr). However, AON12.1-treated YAC128 mice showed activity levels higher or similar to wild-type mice.

Mean + SEM shown. A,B: $N = 10-11$ per group. C,D: $N = 8-11$. E,F: $N = 7-9$. Lower group size in C–F was due to practical and technical issues with phenotyper cages. Mixed effects model for analysis of longitudinal data. Individual timepoints were assessed with Kruskal-Wallis test including post-hoc comparisons using Dunn's multiple testing correction (* $P < 0.05$, ** $P < 0.01$, *** $P < 0.001$).

treated YAC128 mice remained significantly higher compared to aCSF-treated wild-type mice up to 8 months of age as was observed in previous studies (Brooks et al., 2012; Van Raamsdonk et al., 2007; Kuijper et al., 2022; Menalled et al., 2009). Treatment with AON12.1 specifically normalized the body weight of YAC128 mice to wild-type levels, showing no statistical difference from aCSF-treated wild-type animals from 8 months of age.

Motor performance, coordination and balance were investigated using the rotarod. The rotarod revealed a clear phenotype of YAC128 mice from 9 months of age as they showed a significantly shorter latency to fall as described before (Fig. 2B) (Brooks et al., 2012; Van Raamsdonk et al., 2007; Kuijper et al., 2022; Menalled et al., 2009). The phenotype persisted when weight was taken into account (Fig. S8A) and was present as well when we assessed the 'latency to turn around' as some mice stopped running and clung to the rod without falling off during a trial (Fig. S8B). However, AON12.1-treated YAC128 mice did not differ significantly from aCSF-treated YAC128 mice, showing that the shorter latency to fall of YAC128 mice was not restored by AON12.1 treatment.

Hypoactivity has been observed in YAC128 mice before in open field tests and in home cage environment (Slow et al., 2003; Van Raamsdonk et al., 2007; Menalled et al., 2009). In this study, we looked at activity levels of mice during home cage behaviour using phenotyper cages. To give the mice time to adapt to the cage, the activity levels during the second day and night were assessed. During these 24 h, control-treated YAC128 mice showed a lower total distance moved and the time spent in the shelter was higher compared to wild-type mice at both 8 and 11 months, although not significant (Fig. 2C–F, Fig. S9A–D). Treatment with AON12.1 significantly increased the total distance moved and decreased shelter time in YAC128 mice at 8 months and showed a similar trend at 11 months. To ensure that the lower body weight of the AON12.1-treated YAC128 mice was not related to less time spent in the food area of the phenotyper cages, we studied the time spent in the food area relative to the total time spent outside of the shelter but there was no difference between any of the groups (Fig. S9E–F). Furthermore, we assessed anxiety using the light-spot test adapted from Aarts et al. (Aarts et al., 2015) but no phenotype was observed in the YAC128 mice (Fig. S9G–N).

3.3. Striatal volume reduction observed on MRI was attenuated by AON treatment

To study the effect of AON treatment on brain atrophy, we used MRI to determine volumetric changes in YAC128 mice. It became clear that skull deformation, caused by the long-term cannula placement, was

present in 43% of all mice scanned (Fig. S10). Nevertheless, segmentation and analysis could still successfully be performed. First, we assessed the YAC128 phenotype by comparing aCSF-treated wild-type and YAC128 mice. The volume of 4 from the 9 regions assessed (total cerebrum, striatum, pallidum and thalamus) was significantly reduced in YAC128 mice (Fig. 3). No phenotype was found for total cortex, fimbria, corpus callosum, hippocampus and lateral ventricle. Treatment with AON12.1 ameliorated the striatal phenotype in YAC128 mice, showing a higher volume than in aCSF-treated YAC128 mice that did not significantly differ from wild-type striatal volume. However, administration of scrambled AON also showed a similar effect on striatal volume. Scrambled AON seemed to generally increase cerebral volume in YAC128 mice, as the volumes of the cerebrum, thalamus and pallidum were all nonsignificantly increased toward wild-type levels. Enlargement of the lateral ventricles, a side-effect of AON administration described before, was not observed upon treatment with scrambled AON or AON12.1 (Fig. S11) (Tabrizi et al., 2022).

3.4. No reduction of DARPP32 expression was observed in YAC128 mice

To further assess striatal atrophy, we examined expression of DARPP32, a marker for striatal neurons, using immunofluorescence (Fig. 4A). However, no phenotype was observed as staining intensity was similar for aCSF-treated wild-type and YAC128 mice (Fig. 4B). There was one significant difference between the groups, showing a lower DARPP32 expression in AON12.1-treated YAC128 mice compared to aCSF-treated wild-type mice. Nonetheless, this effect of AON treatment was not present in wild-type mice and there was no significant difference between the transgenic groups.

3.5. Treatment with AON reversed HD-related gene expression changes in striatum

Differential gene expression was studied in striatum using RNA sequencing of all YAC128 mice and aCSF-treated wild-type mice (Supplemental File I). We confirmed an HD-related signature in aCSF-treated YAC128 mice compared to aCSF-treated wild-type mice. After genes with low expression levels were filtered out, 11,927 genes were analysed for differential expression (adjusted P -value < 0.1) showing 30 upregulated genes and 38 downregulated genes (Fig. 5A–B). Pathway analysis on up- and downregulated genes separately showed overrepresentation of pathways related with HD such as regulation of gene expression, RNA processing and RNA splicing for upregulated genes and response to stress, signal transduction and axon development for downregulated

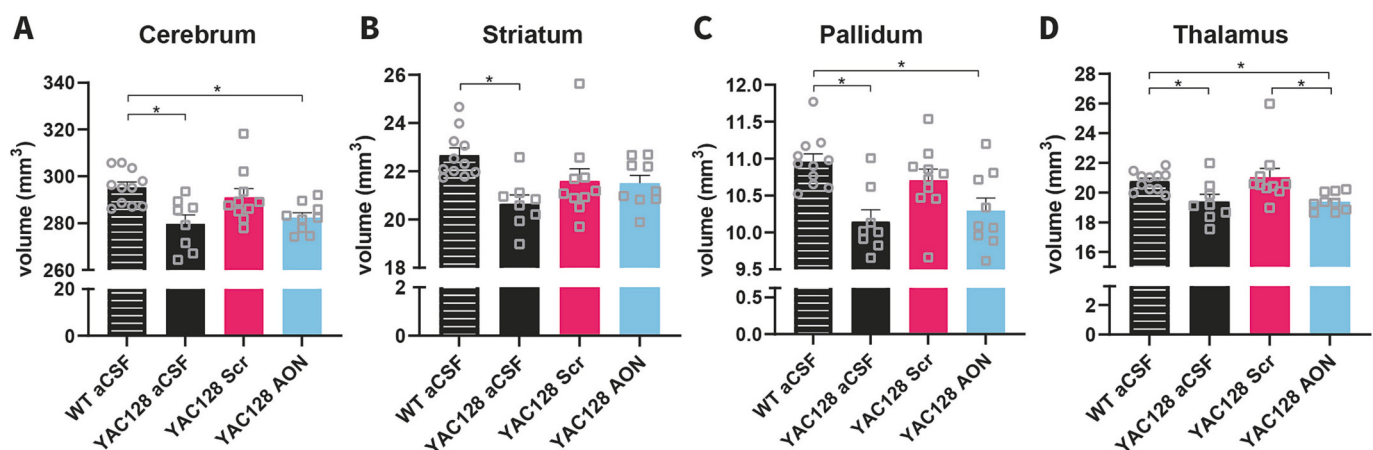


Fig. 3. AON partially attenuated volume reduction in striatum but not pallidum or thalamus.

A–D) As observed with MRI, YAC128 mice had a reduced volume in the whole cerebrum and in striatum, pallidum and thalamus specifically. Treatment with AON12.1 (AON) seemed to specifically improve striatal volume. Administration of scrambled AON (Scr) led to increase of all brain regions. Mean \pm SEM shown. $N = 8$ –11 per group. Kruskal-Wallis test including post-hoc comparisons using Dunn's multiple testing correction ($* P < 0.05$).

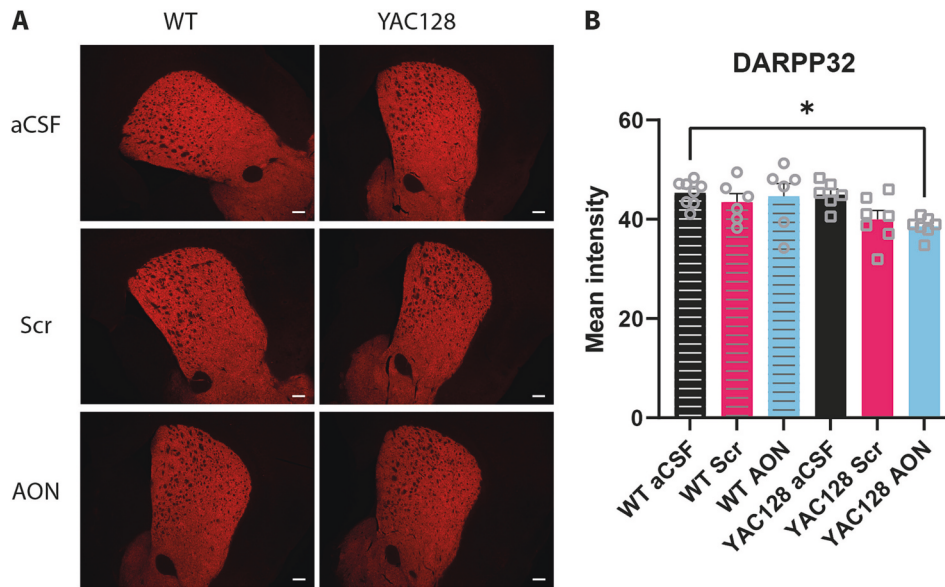


Fig. 4. DARPP32 expression was not reduced in YAC128 mice but was lowered by AON treatment.

A) Representative images of coronal sections stained for DARPP32 are shown for wild-type (WT) and YAC128 mice, treated with aCSF, scrambled AON (Scr) or AON12.1 (AON). B) Quantification of DARPP32 staining in striatum. Scale bar = 200 μ m.

Mean + SEM shown. $N = 6-8$ per group. Kruskal-Wallis test including post-hoc comparisons using Dunn's multiple testing correction (* $P < 0.05$).

genes (Supplemental File II). These findings are in agreement with our previous work where we assessed the disease gene expression signature of YAC128 brain and blood (Kuijper et al., 2022).

Subsequently, we investigated the effect of treatment with AON12.1 on the YAC128 phenotype by comparing the YAC128 aCSF group with the YAC128 AON 12.1 group. Two of the 68 phenotype genes, *Cst3* and *Rab6b*, were significantly reversed upon AON12.1-treatment. Furthermore, many of the 68 up- and downregulated phenotype genes showed changes toward wild-type levels after treatment with AON12.1 although a large variation between mice was observed (Fig. 5A). To investigate which of the 68 phenotype genes were not significantly different from wild-type anymore after treatment, we compared aCSF-treated WT mice and AON12.1-treated YAC128 mice. From the 68 phenotype genes, 18 genes were differentially expressed in the same direction after AON-treatment as in aCSF-treated YAC128 mice, indicating no treatment effect on these genes (Fig. 5C). The remaining 50 of the 68 phenotype genes were not significantly different from aCSF-treated WT mice after treatment with AON indicating a rescue. However, also the scrambled AON had a considerable effect on the expression of the phenotype genes (Fig. 5A). From the 68 phenotype genes, 54 genes were restored (Fig. 5C). We identified 8 phenotype genes that were rescued by AON12.1-treatment and not by the scrambled AON: *Anxa5*, *Car2*, *IL33*, *Pdlim2*, *Penk*, *Qdpr*, *Sgk1* and *Wfs1* (Fig. 5C). One of these genes, *Anxa5*, was upregulated in aCSF-treated YAC128 mice, whereas the other genes showed downregulation. *Car2*, *Qdpr* and *Sgk1* have been associated with myelination (Cammer et al., 1995; de la Fuente et al., 2020; Lim et al., 2022; Licznarski et al., 2015). *Sgk1* is also involved in cellular responses to stress as is *Penk* (Licznarski et al., 2015). *Wfs1* is involved in the response to unfolded proteins and ER and calcium homeostasis (Callens et al., 2022). *Pdlim2* is a cytoskeletal protein that is mainly expressed in oligodendrocytes and microglia in the CNS (Cahoy et al., 2008). *IL33* has a neuroprotective function by suppressing inflammation (Gao et al., 2017a). *Anxa5* plays a role in synaptic transmission (Gotow et al., 1996). As no striatal tissue was left for protein assessment and *Car2* and *IL33* are known to be downregulated in YAC128 cortex as well, we analysed the levels of these two proteins in cortex (Fig. 5D–E, Fig. S12) (Kuijper et al., 2022). We observed a downregulation of both *Car2* and *IL33* that was ameliorated by AON12.1. However, scrambled AON also slightly increased expression in YAC128 mice.

3.6. AON12.1-specific gene expression changes were related to various pathways such as metabolism, signalling and transcriptional regulation

The AON-related expression changes were elaborate and went beyond the 68 HD signature genes (Fig. 5B–C). These AON-related expression changes could be classified as either an AON12.1-specific, biological compensation of YAC128 pathology, or be a non-specific reaction to the presence of an AON. Hence, we further studied AON-related changes by comparing gene expression changes in the YAC128 mice treated with scrambled AON or AON12.1. First, we assessed the genes differentially expressed between YAC128 mice treated with scrambled AON or AON12.1. Five genes were downregulated upon AON12.1 treatment: *Nalcn*, *Nrip3*, *Alkbh6*, *Rnf157* and *2900060N12Rik*. The function of *2900060N12Rik* is still unknown, but *Nalcn* is involved in ion transport (Cochet-Bissuel et al., 2014), *Nrip3* is involved in proteolysis and its expression is induced by BDNF (Koshimizu et al., 2021). *Alkbh6* is involved in DNA repair and E3 ligase *Rnf157* seemed to promote cell survival (Matz et al., 2015; Zhao et al., 2021; Ma et al., 2022). Genes upregulated by AON12.1 were: *Igtb4*, *Gsn*, *Gab1*, *Trf*, *Dcdc2a*, *H1-f2*, *Zfp672*, *Gas5*, *Cd302*, *C4b*, *1110038B12Rik* and *Gm11942*. These genes are involved in oligodendrocyte function (*Gab1*, *Trf*), apoptosis (*Gsn*, *H1-f2*, *Gas5*), immune cell activity (*C4b*, *Cd302*), neuronal migration (*Dcdc2a*), extracellular matrix organization (*Igtb4*), muscle wasting (*1110038B12Rik*) and transcriptional regulation (*Zfp672*) (Zhao et al., 2018; Wang et al., 2021; Tshilenge et al., 2023; Xu et al., 2022; Fatoba et al., 2022; Ziabska et al., 2021; Meng et al., 2020; Gao et al., 2017b; Zhou et al., 2020; Espinosa-Jeffrey et al., 2002; Weinzimmer et al., 2001; Konishi et al., 2003; Lo et al., 2016).

Subsequently, we selected the genes altered by AON12.1 or scrambled AON compared to wild-type or YAC128 aCSF-treated mice that were not part of the 68 HD signature genes (Table S3–S4) and performed pathway analysis on the up- and downregulated genes separately (Table 3, Table S5–S6, Supplemental File III). Upregulation by AON12.1 but not by scrambled AON reflected an adaptive immune response but also glutamatergic synaptic transmission and regulation of transcription and splicing. Downregulated genes by AON12.1 showed specific enrichment of metabolic pathways such as cellular respiration and fatty acid metabolism and regulation of signalling, ion homeostasis and regulation of growth. A non-specific AON reaction was evident in the

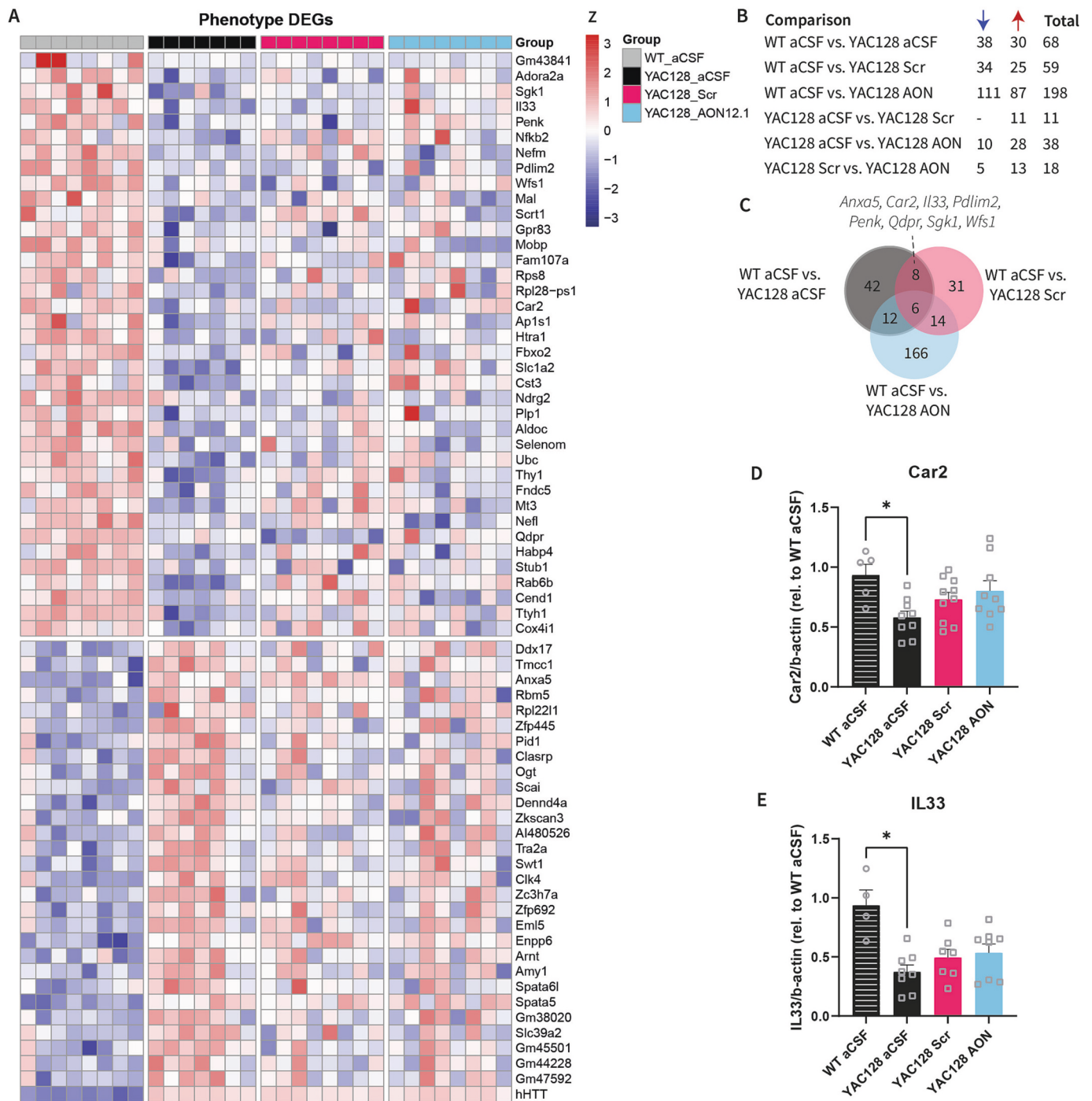


Fig. 5. Striatal gene expression changes showed reversal by AON treatment.

A) Heatmap of 38 downregulated and 30 upregulated genes in aCSF-treated YAC128 mice compared to aCSF-treated wild-type mice showed that both treatment with AON12.1 and scrambled AON (Scr) reversed expression toward wild-type levels for many genes, although large within-group variation was observed. B) Number of genes significantly up- and downregulated (FDR < 0.1) for all pairwise comparisons. C) Comparison of deregulated genes in different YAC128 groups demonstrated 8 genes rescued specifically by AON12.1 (AON) treatment. D–E) Two genes rescued by AON12.1 in striatum showed a similar phenotype and rescue on protein level in cortex. Scrambled AON seemed to partially restore Car2 and IL33 levels.

A–C: N = 7–8 per group. D–E: Mean + SEM shown. N = 5–10 (D) and N = 4–8 (E) per group. Kruskal-Wallis test including post-hoc comparisons using Dunn's multiple testing correction (* P < 0.05).

pathways shared between AON12.1 and scrambled AON enriched within upregulated genes, showing for instance leukocyte migration and activation, glial cell development and regulation of cell death. Shared pathways based on downregulated genes were associated with protein localization and cellular component organization.

Finally, as we observed a decreased staining of DARPP32 in striata of

YAC128 mice upon treatment with AON12.1, we looked at DARPP32 expression on RNA level. Here, we did not observe differences between the groups. There was also no difference for *Drd1* and *Drd2*, genes specific for various types of medium spiny neurons as well. In addition, expression of apoptosis-related genes *Bcl-2* and *Bax* was not altered. Although the regulation of cell death was enriched among AON12.1-

Table 3

Representative overview of pathways enriched within up- and downregulated genes upon treatment with scrambled AON or AON12.1 that were not related to the YAC128 phenotype, including the implicated genes.

Pathway	Scrambled AON	AON12.1
Upregulated genes unrelated to YAC128 phenotype		
Complement activation	C1qa, C1qb	–
Defense response	B2m, C1qa, C1qb, Lyz2	B2m, C1qb, Cd74, Chst1, Cyld, Fcer1g, H2-K1, Ifitm3, Kalrn, Lyz2, Tac1, Tnfrsf1a
Positive regulation of immune response	B2m, C1qa, C1qb, Calr, Tyrobp, Grn	B2m, C1qb, C4b, Cd74, Cyld, Fcer1g, H2-D1, H2-K1, Ripor2, Shb, Tac1, Tyrobp
Cell motility and adhesion	Ap1ar, Apod, Calr, Grn, Dscaml1, Smoc1, Tnem3	Ap1ar, Apod, Cd74, Cyld, Gsn, Ptk2, Ripor2, Shb, Smoc1, Tac1, Trf, Vim
(Regulation of) cell death	C1qa, Grn, S100b, Tyrobp	Agap2, Ccnd2, Cd74, Cyld, Fcer1g, Gsn, Ptk2, S100b, Sox8, Tac1, Tnfrsf1a, Tyrobp, Ybx1, Kremen1, Shb, Taok1
Adaptive immune response and antigen presentation	–	B2m, Cd74, Fcer1g, H2-D1, H2-K1, C4b
Regulation of transcription	–	Agap2, Cbx4, Cd74, Cyld, H1f2, Ifi27, Sox8, Tnfrsf1a, Trf, Trrap, Ybx1
Regulation of splicing	–	Hnrnp1, Rbfox1, Rps26
Glutamatergic signalling	–	Cdh8, Gria2, Hnrnp1, Itgb4, Rimb2, Tac1
Downregulated genes unrelated to YAC128 phenotype		
Establishment of protein localization	Nsg1, Reep1, Stx1b, Tbc1d9b	Agt, Cbln1, Rph3a, Sncg, Tmed3, Unc119, Ywhaz, Zdhc22
Cellular component organization	Atxn10, Hprt, Nsg1, Reep1, Stx1b, Tspan2, Zwint	Ache, Agt, Atp5d, Atp6v0d1, Atxn10, Chchd6, Cirbp, Coq7, Gjb6, H1f10, Kcnj10, Kctd2, Mrpl17, Ndufs7, Ppia, Rph3a, Slc25a4, Slc25a5, Sncb, Sncg, Tlcl1, Tmed3, Tubb3, Vamp1, Ywhaz
Cellular respiration and mitochondrial ATP synthesis	–	Atp5d, Ndufs7, Coq7, Ndufv1
Fatty acid metabolism	–	Fads1, Prxl2b, Ptgds, Tecr
Regulation of signalling	–	Ache, Agt, Bend6, Calb2, Cbln1, Enho, Fbxo9, Fzd2, Kcnj10, Lynx1, Ntsr2, Rims3, Rph3a, Sfrp5, Slc25a5, Sncg, Tle5, Vamp1
Ion homeostasis	–	Agt, Atp1a2, Atp1b3, Atp6v0d1, Calb2, Fzd2, Kcnj10, Ndfip1, Tlcl1
Ion transport	–	Atp1a2, Atp1b3, Atp5d, Atp6v0d1, Kcnip4, Kcnj10, Nalcn, Ndfip1, Ndufs7, Slc17a6, Slc1a6, Slc25a4, Ywhaz
Regulation of growth	–	Agt, Cirbp, Gamt, Rnf157, Rpl4, Sfrp5, Slc25a4, Tkt, Tle5

mediated expression changes, both anti-apoptotic and pro-apoptotic genes were upregulated. *Aif1* expression levels were not altered upon AON administration suggesting there was no microglial response. However, an increase in *Gfap* expression was observed both upon administration of scrambled AON and AON12.1 suggesting a reaction of astrocytes to the presence of the AON (Fig. S13).

4. Discussion

In HD, a wide variety of disease mechanisms have been identified including the generation of protein fragments from the mutant HTT protein by proteolytic cleavage. In this study, we aimed to ameliorate the toxicity of mutant HTT in YAC128 mice by modifying the HTT

protein in order to reduce proteolytic cleavage by caspase-6 while leaving HTT protein levels intact. To that end, we used an AON that targets HTT pre-mRNA and induces partial skipping of exon 12, thereby removing the critical caspase-6 site.

We confirmed successful exon skipping in both cortex and cerebellum and around 40% protein modification in the cortex while total levels of hHTT were not changed. AON treatment was able to rescue part of the behavioural phenotype observed in this model for HD. This was in line with other studies in YAC128 mice achieving reduced N586-HTT levels by genetically ablating caspase-6 or removing the caspase-6 motif from HTT (Graham et al., 2006; Pouladi et al., 2009; Wong et al., 2015). We observed that treatment with AON12.1 normalized the body weight of YAC128 mice to wild-type levels within a month, an effect that lasted until the end of the study. In addition, the hypoactivity observed in YAC128 mice was restored by AON treatment however the phenotype observed on the rotarod was not rescued. The increased body weight in YAC128 mice is a common feature of models overexpressing full-length *HTT* and is thought to be mediated by IGF-1 levels (Pouladi et al., 2010; Van Raamsdonk et al., 2006). We observed AON-induced gene expression changes related to metabolic pathways and upregulation of IGF-related genes (Trf, C4b) that might partially explain the reduction of body weight. The persistence of the rotarod phenotype in AON-treated YAC128 mice could suggest that about 40% protein modification is not enough to improve this phenotype or could be due to irreversible changes at 6 months of age when treatment started, requiring earlier treatment.

Gene expression analysis in striatum revealed a rescue of 8 genes dysregulated in YAC128 mice by AON12.1: *Anxa5*, *Car2*, *IL33*, *Pdlim2*, *Penk*, *Qdpr*, *Sgk1* and *Wfs1*. Dysregulation of several of these genes has been robustly shown before in mouse models for HD or patient CSF (Kuijper et al., 2022; Licznarski et al., 2015; Bissonnette et al., 2013; Barschke et al., 2022). In addition, AON12.1 changed expression of genes involved in HD-related processes such as glutamatergic signalling, regulation of transcription and splicing, ion transport and cellular metabolism. Together, these gene expression changes represent a beneficial effect of AON12.1 treatment. Our findings validate a previous study where overexpression of *Penk* in R6/2 mice ameliorated behavioural symptoms (Bissonnette et al., 2013).

In addition, striatal gene expression analysis showed activation of genes involved in innate immune-related pathways by both scrambled AON and AON12.1, a general response we have observed before in mice treated ICV with 2'-O-methyl phosphorothioate AONs (Toonen et al., 2018). As the scrambled AON also had a beneficial effect on the HD-related gene expression changes, this general inflammatory response might contribute to the rescue of HD-related processes. AON12.1 also increased expression of genes related to adaptive immunity, showing enrichment of genes related to T-cell and B-cell activation and antigen presentation. As our strategy involves generation of a novel protein, a potential autoimmune response must be kept in mind.

MRI analysis demonstrated that striatal volume reduction seemed to be attenuated by AON treatment. No enlargement of the lateral ventricle was observed, a side effect described upon administration of for instance the gapmer AON tominersen (Tabrizi et al., 2022). However, scrambled AON seemed to cause general brain enlargement that, to our knowledge, has not been described before. Most studies involving AON administration include either a vehicle or scrambled control and hence do not allow assessment of the scrambled AON. Our data for both gene expression and brain anatomy showed a significant effect of scrambled AON, emphasizing the importance of including scrambled AONs in treatment studies to better understand the effect of exposure of the brain to AON compounds, regardless of their sequence.

Our study was limited by the mild phenotype present in YAC128/B6 mice, which did not show striatal neuronal death reflected by DARPP32 expression. A milder phenotype of YAC128 mice on B6 compared to FVB/N background has been described before (Van Raamsdonk et al., 2007). However, susceptibility for epileptic seizures in FVB/N mice

made this strain unpreferable for this study as multiple ICV injections needed for AON administration would likely result in unacceptable suffering and mortality.

The therapeutic strategy we propose is not affecting the N-terminal HTT fragments produced by alternative splicing, involving the use of an alternative polyA-site in intron 1, leading to the expression of HTT exon 1 (Neueder et al., 2017; Sathasivam et al., 2013). The extent of the contribution of HTT-exon1 to HD pathology is yet unknown. However, our results confirm findings from previous studies (Graham et al., 2006; Pouladi et al., 2009; Wong et al., 2015) demonstrating that lowering the formation of toxic N-terminal fragments by targeting the rate-limiting caspase-6 cleavage step is sufficient to ameliorate the HD phenotype in YAC128 mice.

To further assess the therapeutic potential of AON12.1, it should be tested in an additional mouse model that does display decreased DARPP32 levels such as the humanized Hu128/21 mice (Southwell et al., 2017). The use of a humanized mouse model would also rule out the effect of endogenous mouse *Htt* expression. Furthermore, an earlier start of treatment should be tested to see whether early phenotypes such as the rotarod could be restored as well. In addition, toxicity studies are needed to ensure AON safety.

In conclusion, we showed that AON12.1-mediated modification of mutant HTT demonstrates a beneficial effect on YAC128 body weight, activity levels, striatal volume and striatal gene expression, adding to the study by Kim et al. that showed that this AON sequence could improve the molecular phenotype in YAC128 mice (Kim et al., 2022). We did not observe negative effects of AON12.1 treatment except for a minor reduction in DARPP32 expression in striatum. Finally, while the treatment effect on body weight and activity was specific for AON12.1, the effect of the scrambled AON on the HD striatal gene signature and brain volume showed that it is essential to take along a scrambled control to correct for non-specific AON-related effects. Further investigation on AON-related downstream effects affecting HD should enlighten the safety and potential use in human treatment.

Supplementary data to this article can be found online at <https://doi.org/10.1016/j.nbd.2023.106368>.

CRedit authorship contribution statement

Elsa C. Kuijper: Conceptualization, Formal analysis, Investigation, Methodology, Project administration, Visualization, Writing – original draft. **Maurice Overzier:** Investigation. **Ernst Suidgeest:** Investigation, Writing – review & editing. **Oleh Dzyubachyk:** Investigation, Writing – review & editing. **Cécile Maguin:** Investigation, Writing – review & editing. **Jean-Baptiste Pérot:** Investigation, Writing – review & editing. **Julien Flament:** Investigation, Writing – review & editing. **Yavuz Ariyurek:** Investigation, Writing – review & editing. **Hailiang Mei:** Investigation, Writing – review & editing. **Ronald A.M. Buijsen:** Methodology, Writing – review & editing. **Louise van der Weerd:** Methodology, Writing – review & editing. **Willeke van Roon-Mom:** Conceptualization, Funding acquisition, Methodology, Project administration, Supervision, Writing – review & editing.

Declaration of Competing Interest

WvRM discloses being employed by LUMC which has patents on exon skipping approaches for neurological disorders. In the past, some of these patents have been licensed to ProQR therapeutics. As co-inventor on these patents WvRM is entitled to a share of milestone payments and royalties. WvRM further discloses being *ad hoc* consultant for Accure Therapeutics and Herbert Smith Freehills. Remuneration for these activities is paid to the LUMC. LUMC also received funding for contract research from UniQure and Amylon Therapeutics. RAMB is member of the Scientific Advisory Council of the Oligonucleotide Therapeutics Society. ECK, MO, ES, OD, CM, JBP, JF, YA, HM and LvdW declare no conflict of interest.

Data availability

Raw RNAseq data generated in this paper are available in the GEO repository, GSE239312. The R script used for the analysis of the RNAseq data is available upon request.

Acknowledgements

This work was funded by CampagNETeam Huntington. The authors would like to thank Lodewijk Toonen for his contribution to setting up the *in vivo* study, Jelle Goeman for advice on statistical analysis and ProQR Therapeutics NV for providing the AONs and regular discussions within the shared CampagNETeam Huntington grant.

References

- Aarts, E., Maroteaux, G., Loos, M., Koopmans, B., Kovačević, J., Smit, A.B., et al., 2015. The light spot test: measuring anxiety in mice in an automated home-cage environment. *Behav. Brain Res.* 294, 123–130.
- Bagnoli, J.W., Ziegenhain, C., Janjic, A., Wange, L.E., Vieth, B., Parekh, S., et al., 2018. Sensitive and powerful single-cell RNA sequencing using mcSCR-seq. *Nat. Commun.* 9 (1), 2937.
- Barschke, P., Abu-Rumeileh, S., Al Shweiki, M., Barba, L., Paolini Paoletti, F., Oeckl, P., et al., 2022. Cerebrospinal fluid levels of proenkephalin and prodynorphin are differentially altered in Huntington's and Parkinson's disease. *J. Neurol.* 269 (9), 5136–5143.
- van der Bent, M.L., Evers, M.M., Valles, A., 2022. Emerging therapies for Huntington's disease - focus on N-terminal huntingtin and huntingtin exon 1. *Biologics.* 16, 141–160.
- Bissonnette, S., Vaillancourt, M., Hébert, S.S., Drolet, G., Samadi, P., 2013. Striatal pre-enkephalin overexpression improves Huntington's disease symptoms in the R6/2 mouse model of Huntington's disease. *PLoS One* 8 (9), e75099.
- Brooks, S., Higgs, G., Janghra, N., Jones, L., Dunnett, S.B., 2012. Longitudinal analysis of the behavioural phenotype in YAC128 (C57BL/6J) Huntington's disease transgenic mice. *Brain Res. Bull.* 88 (2–3), 113–120.
- Cahoy, J.D., Emery, B., Kaushal, A., Foo, L.C., Zamanian, J.L., Christopherson, K.S., et al., 2008. A transcriptome database for astrocytes, neurons, and oligodendrocytes: a new resource for understanding brain development and function. *J. Neurosci.* 28 (1), 264–278.
- Callens, M., Loncke, J., Bultynck, G., 2022. Dysregulated Ca²⁺ Homeostasis as a Central Theme in Neurodegeneration: Lessons from Alzheimer's Disease and Wolfram Syndrome. *11* (12), 1963.
- Cammer, W., Zhang, H., Tansey, F.A., 1995. Effects of carbonic anhydrase II (CAII) deficiency on CNS structure and function in the myelin-deficient CAII-deficient double mutant mouse. *J. Neurosci. Res.* 40 (4), 451–457.
- Capaldi, D.C., Scozzari, A.N., 2007. Manufacturing and analytical processes for 2'-O-(2-Methoxyethyl)-modified oligonucleotides. In: *Antisense Drug Technology Principles, Strategies, and Applications*, 2 ed. CRS Press, New York.
- Casaca-Carreira, J., Toonen, L.J.A., Evers, M.M., Jahanshahi, A., van Roon-Mom WMC, Temel Y., 2016. In vivo proof-of-concept of removal of the huntingtin caspase cleavage motif-encoding exon 12 approach in the YAC128 mouse model of Huntington's disease. *Biomedicine & Pharmacotherapy = Biomedicine & Pharmacotherapie.* 84, 93–96.
- Celestine, M., Nadkarni, N.A., Garin, C.M., Bougacha, S., Dhenain, M., 2020. Samba-MRI: A Library for Processing Small-Mammal Brain MRI Data in Python. *Front. Neuroinform.* 14, 24.
- Cochet-Bissuel, M., Lory, P., Monteil, A., 2014. The sodium leak channel, NALCN, in health and disease. *Front. Cell. Neurosci.* 8, 132.
- Cox, R.W., 1996. AFNI: software for analysis and visualization of functional magnetic resonance neuroimages. *Computers Biomed. Res. Int. J.* 29 (3), 162–173.
- Dietrich, P., Johnson, I.M., Alli, S., Dragatsis, I., 2017. Elimination of huntingtin in the adult mouse leads to progressive behavioral deficits, bilateral thalamic calcification, and altered brain iron homeostasis. *PLoS Genet.* 13 (7), e1006846.
- DiFiglia, M., Sapp, E., Chase, K.O., Davies, S.W., Bates, G.P., Vonsattel, J.P., et al., 1997. Aggregation of huntingtin in neuronal intranuclear inclusions and dystrophic neurites in brain. *Science.* 277 (5334), 1990–1993.
- Dzyubachyk, O., Tao, Q., Poot, D.H.J., Lamb, H.J., Zeppenfeld, K., Lelieveldt, B.P.F., et al., 2015. Super-resolution reconstruction of late gadolinium-enhanced MRI for improved myocardial scar assessment. *42* (1), 160–167.
- Ehrnhofer, D.E., Skotte, N.H., Reinshagen, J., Qiu, X., Windshugel, B., Jaishankar, P., et al., 2019. Activation of Caspase-6 is promoted by a mutant huntingtin fragment and blocked by an allosteric inhibitor compound. *Cell. Chem. Biol.* 26 (9), 1295–305 e6.
- El-Daher, M.T., Hangen, E., Bruyere, J., Poizat, G., Al-Ramahi, I., Pardo, R., et al., 2015. Huntingtin proteolysis releases non-polyQ fragments that cause toxicity through dynamin 1 dysregulation. *EMBO J.* 34 (17), 2255–2271.
- Espinosa-Jeffrey, A., Kumar, S., Zhao, P.M., Awosika, O., Agbo, C., Huang, A., et al., 2002. Transferrin regulates transcription of the MBP gene and its action synergizes with IGF-1 to enhance myelinogenesis in the md rat. *Dev. Neurosci.* 24 (2–3), 227–241.

- Espinosa-Oliva, A.M., Garcia-Revilla, J., Alonso-Bellido, I.M., Burguillos, M.A., 2019. Brainiac caspases: beyond the wall of apoptosis. *Front. Cell. Neurosci.* 13, 500.
- Evers, M.M., Tran, H.D., Zalachoras, I., Meijer, O.C., den Dunnen, J.T., van Ommen, G.J., et al., 2014. Preventing formation of toxic N-terminal huntingtin fragments through antisense oligonucleotide-mediated protein modification. *Nucleic Acid Ther.* 24 (1), 4–12.
- Farshim, P.P., Bates, G.P., 2018. Mouse models of Huntington's disease. In: Precious, S. V., Rosser, A.E., Dunnett, S.B. (Eds.), *Huntington's Disease*. Springer New York, New York, NY, pp. 97–120.
- Fatoba, O., Itokazu, T., Yamashita, T., 2022. Complement cascade functions during brain development and neurodegeneration. *289 (8)*, 2085–2109.
- de la Fuente, A.G., Queiroz, R.M.L., Ghosh, T., McMurrin, C.E., Cubillos, J.F., Bergles, D. E., et al., 2020. Changes in the oligodendrocyte progenitor cell proteome with ageing. *Mol. Cell. Proteomic. MCP.* 19 (8), 1281–1302.
- Gao, J., Qin, Z., Guan, X., Guo, J., Wang, H., Liu, S., 2017b. Overexpression of GSN could decrease inflammation and apoptosis in EAE and may enhance vitamin D therapy on EAE/MS. *Sci. Rep.* 7 (1), 604.
- Gao, Y., Luo, C.L., Li, L.L., Ye, G.H., Gao, C., Wang, H.C., et al., 2017a. IL-33 provides neuroprotection through suppressing apoptosis, Autophagic and NF- κ B-mediated inflammatory pathways in a rat model of recurrent neonatal seizure. *Front. Mol. Neurosci.* 10, 423.
- Gerstner, N., Kehl, T., Lenhof, K., Müller, A., Mayer, C., Eckhart, L., et al., 2020. GeneTrail 3: advanced high-throughput enrichment analysis. *Nucleic Acids Res.* 48 (W1), W515–W520.
- Gotow, T., Sakata, M., Funakoshi, T., Uchiyama, Y., 1996. Preferential localization of annexin V to the axon terminal. *Neuroscience.* 75 (2), 507–521.
- Graham, R.K., Deng, Y., Slow, E.J., Haigh, B., Bissada, N., Lu, G., et al., 2006. Cleavage at the caspase-6 site is required for neuronal dysfunction and degeneration due to mutant huntingtin. *Cell.* 125 (6), 1179–1191.
- Jansen, A.H.P., van Hal, M., op den Kelder, I.C., Meier, R.T., de Ruiter, A.-A., Schut, M. H., et al., 2017. Frequency of nuclear mutant huntingtin inclusion formation in neurons and glia is cell-type-specific. *65 (1)*, 50–61.
- Kenkhuus, B., van Eekeren, M., Parfitt, D.A., Ariyurek, Y., Banerjee, P., Priller, J., et al., 2022. Iron accumulation induces oxidative stress, while depressing inflammatory polarization in human iPSC-derived microglia. *Stem Cell Rep.* 17 (6), 1351–1365.
- Kim, H., Lenoir, S., Helfricht, A., Jung, T., Karneva, Z.K., Lee, Y., et al., 2022. A pathogenic proteolysis-resistant huntingtin isoform induced by an antisense oligonucleotide maintains huntingtin function. *JCI Insight.* 7 (17).
- Kingwell, K., 2021. Double setback for ASO trials in Huntington disease. *Nat. Rev. Drug Discov.* 20 (6), 412–413.
- Konishi, A., Shimizu, S., Hirota, J., Takao, T., Fan, Y., Matsuoka, Y., et al., 2003. Involvement of histone H1.2 in apoptosis induced by DNA double-strand breaks. *Cell.* 114 (6), 673–688.
- Kordasiewicz Holly, B., Stanek Lisa, M., Wanczewicz Edward, V., Mazur, C., McAlonis Melissa, M., Pytel Kimberly, A., et al., 2012. Sustained therapeutic reversal of Huntington's disease by transient repression of huntingtin synthesis. *Neuron.* 74 (6), 1031–1044.
- Koshimizu, H., Matsuoka, H., Nakajima, Y., Kawai, A., Ono, J., Ohta, K.I., et al., 2021. Brain-derived neurotrophic factor predominantly regulates the expression of synapse-related genes in the striatum: insights from in vitro transcriptomics. *Neuropsychopharmacol. Rep.* 41 (4), 485–495.
- Kuijper, E.C., Toonen, L.J.A., Overzier, M., Tsonaka, R., Hettne, K., Roos, M., et al., 2022. Huntington disease gene expression signatures in blood compared to brain of YAC128 mice as candidates for monitoring of pathology. *Mol. Neurobiol.* 59 (4), 2532–2551.
- Landles, C., Sathasivam, K., Weiss, A., Woodman, B., Moffitt, H., Finkbeiner, S., et al., 2010. Proteolysis of mutant huntingtin produces an exon 1 fragment that accumulates as an aggregated protein in neuronal nuclei in Huntington disease. *J. Biol. Chem.* 285 (12), 8808–8823.
- Lein, E.S., Hawrylycz, M.J., Ao, N., Ayres, M., Bensinger, A., Bernard, A., et al., 2007. Genome-wide atlas of gene expression in the adult mouse brain. *Nature.* 445 (7124), 168–176.
- Licznerski, P., Duric, V., Banasr, M., Alavian, K.N., Ota, K.T., Kang, H.J., et al., 2015. Decreased SGK1 expression and function contributes to behavioral deficits induced by traumatic stress. *PLoS Biol.* 13 (10), e1002282.
- Lim, R.G., Al-Dalahmah, O., Wu, J., Gold, M.P., Reidling, J.C., Tang, G., et al., 2022. Huntington disease oligodendrocyte maturation deficits revealed by single-nucleus RNAseq are rescued by thiamine-biotin supplementation. *Nat. Commun.* 13 (1), 7791.
- Lo, T.H., Silveira, P.A., Fromm, P.D., Verma, N.D., Vu, P.A., Kupresanin, F., et al., 2016. Characterization of the expression and function of the C-type lectin receptor CD302 in mice and humans reveals a role in dendritic cell migration. *J. Immunol.* 197 (3), 885–898.
- Ma, L., Lu, H., Tian, Z., Yang, M., Ma, J., Shang, G., et al., 2022. Structural insights into the interactions and epigenetic functions of human nucleic acid repair protein ALKBH6. *J. Biol. Chem.* 298 (3), 101671.
- Matz, A., Lee, S.J., Schwedhelm-Domeyer, N., Zanini, D., Holubowska, A., Kannan, M., et al., 2015. Regulation of neuronal survival and morphology by the E3 ubiquitin ligase RNF157. *Cell Death Differentiation.* 22 (4), 626–642.
- Menalled, L., El-Khodori, B.F., Patry, M., Suarez-Farinan, M., Orenstein, S.J., Zahasky, B., et al., 2009. Systematic behavioral evaluation of Huntington's disease transgenic and knock-in mouse models. *Neurobiol. Dis.* 35 (3), 319–336.
- Mende-Mueller, L.M., Toneff, T., Hwang, S.R., Chesselet, M.F., Hook, V.Y., 2001. Tissue-specific proteolysis of huntingtin (htt) in human brain: evidence of enhanced levels of N- and C-terminal htt fragments in Huntington's disease striatum. *J. Neurosci.* 21 (6), 1830–1837.
- Meng, X., Liu, P., Wu, Y., Liu, X., Huang, Y., Yu, B., et al., 2020. Integrin beta 4 (ITGB4) and its tyrosine-1510 phosphorylation promote pancreatic tumorigenesis and regulate the MEK1-ERK1/2 signaling pathway. *Bosn. J. Basic Med. Sci.* 20 (1), 106–116.
- Metz, T., Kuijper, E.C., van Roon-Mom, W.M.C., 2022. Delivery of antisense oligonucleotides to the mouse brain by Intracerebroventricular injections. *Methods in Molecular Biology (Clifton, NJ)*. 2434, 333–341.
- Neueder, A., Landles, C., Ghosh, R., Howland, D., Myers, R.H., Faull, R.L.M., et al., 2017. The pathogenic exon 1 HTT protein is produced by incomplete splicing in Huntington's disease patients. *Sci. Rep.* 7 (1), 1307.
- Nopoulos, P.C., 2016. Huntington disease: a single-gene degenerative disorder of the striatum. *Dialogues Clin. Neurosci.* 18 (1), 91–98.
- Oguz, I., Zhang, H., Rumpel, A., Sonka, M., 2014. RATS: rapid automatic tissue segmentation in rodent brain MRI. *J. Neurosci. Methods* 221, 175–182.
- Palaiogeorgou, A.M., Papakonstantinou, E., Golfiopoulou, R., Sigala, M., Mitsis, T., Papageorgiou, L., et al., 2023. Recent approaches on Huntington's disease (review). *Biomed Rep.* 18 (1), 5.
- Pérot, J.B., Célestine, M., Palombo, M., Dhenain, M., Humbert, S., Brouillet, E., et al., 2022. Longitudinal multimodal MRI characterization of a knock-in mouse model of Huntington's disease reveals early gray and white matter alterations. *Hum. Mol. Genet.* 31 (21), 3581–3596.
- Pouladi, M.A., Graham, R.K., Karasinska, J.M., Xie, Y., Santos, R.D., Petersen, A., et al., 2009. Prevention of depressive behaviour in the YAC128 mouse model of Huntington disease by mutation at residue 586 of huntingtin. *Brain.* 132 (Pt 4), 919–932.
- Pouladi, M.A., Xie, Y., Skotte, N.H., Ehrnhoefer, D.E., Graham, R.K., Kim, J.E., et al., 2010. Full-length huntingtin levels modulate body weight by influencing insulin-like growth factor 1 expression. *Hum. Mol. Genet.* 19 (8), 1528–1538.
- Rüb, U., Seidel, K., Heinsen, H., Vonsattel, J.P., den Dunnen, W.F., Korf, H.W., 2016. Huntington's disease (HD): the neuropathology of a multisystem neurodegenerative disorder of the human brain. *Brain pathology (Zurich, Switzerland)*. 26 (6), 726–740.
- Sathasivam, K., Neueder, A., Gipson, T.A., Landles, C., Benjamin, A.C., Bondulich, M.K., et al., 2013. Aberrant splicing of HTT generates the pathogenic exon 1 protein in Huntington disease. *Proc. Natl. Acad. Sci. U. S. A.* 110 (6), 2366–2370.
- Slow, E.J., van Raamsdonk, J., Rogers, D., Coleman, S.H., Graham, R.K., Deng, Y., et al., 2003. Selective striatal neuronal loss in a YAC128 mouse model of Huntington disease. *Hum. Mol. Genet.* 12 (13), 1555–1567.
- Southwell, A.L., Skotte, N.H., Villanueva, E.B., Østergaard, M.E., Gu, X., Kordasiewicz, H. B., et al., 2017. A novel humanized mouse model of Huntington disease for preclinical development of therapeutics targeting mutant huntingtin alleles. *Hum. Mol. Genet.* 26 (6), 1115–1132.
- Stéphane, D.G., Guy, E., Michel, K., François, S.R., 2016. The FVB/N mice: a well suited strain to study learning and memory processes using olfactory cues. *Behav. Brain Res.* 296, 254–259.
- Tabrizi, S.J., Estevez-Fraga, C., van Roon-Mom, W.M.C., Flower, M.D., Scahill, R.I., Wild, E.J., et al., 2022. Potential disease-modifying therapies for Huntington's disease: lessons learned and future opportunities. *Lancet Neurol.* 21 (7), 645–658.
- Tebbenkamp, A.T., Green, C., Xu, G., Denovan-Wright, E.M., Rising, A.C., Fromholt, S.E., et al., 2011. Transgenic mice expressing caspase-6-derived N-terminal fragments of mutant huntingtin develop neurologic abnormalities with predominant cytoplasmic inclusion pathology composed largely of a smaller proteolytic derivative. *Hum. Mol. Genet.* 20 (14), 2770–2782.
- Teo, R.T., Hong, X., Yu-Taeger, L., Huang, Y., Tan, L.J., Xie, Y., et al., 2016. Structural and molecular myelination deficits occur prior to neuronal loss in the YAC128 and BACHD models of Huntington disease. *Hum. Mol. Genet.* 25 (13), 2621–2632.
- Toonen, L.J.A., Casaca-Carreira, J., Pellisé-Tintoré, M., Mei, H., Temel, Y., Jahanshahi, A., et al., 2018. Intracerebroventricular administration of a 2'-O-methyl Phosphorothioate antisense oligonucleotide results in activation of the innate immune system in mouse brain. *Nucleic Acid Therapeutics.* 28 (2), 63–73.
- Tshilenge, K.-T., Aguirre, C.G., Bons, J., Gerencser, A.A., Basisty, N., Song, S., et al., 2023. Proteomic Analysis of Huntington's Disease Medium Spiny Neurons Identifies Alterations in Lipid Droplets. *Mol. Cell. Proteomics* 22 (5).
- Uribe, V., Wong, B.K., Graham, R.K., Cusack, C.L., Skotte, N.H., Pouladi, M.A., et al., 2012. Rescue from excitotoxicity and axonal degeneration accompanied by age-dependent behavioral and neuroanatomical alterations in caspase-6-deficient mice. *Hum. Mol. Genet.* 21 (9), 1954–1967.
- Van Raamsdonk, J.M., Gibson, W.T., Pearson, J., Murphy, Z., Lu, G., Leavitt, B.R., et al., 2006. Body weight is modulated by levels of full-length huntingtin. *Hum. Mol. Genet.* 15 (9), 1513–1523.
- Van Raamsdonk, J.M., Metzler, M., Slow, E., Pearson, J., Schwab, C., Carroll, J., et al., 2007. Phenotypic abnormalities in the YAC128 mouse model of Huntington disease are penetrant on multiple genetic backgrounds and modulated by strain. *Neurobiol. Dis.* 26 (1), 189–200.
- Waldron-Roby, E., Ratovitski, T., Wang, X., Jiang, M., Watkin, E., Arbez, N., et al., 2012. Transgenic mouse model expressing the caspase 6 fragment of mutant huntingtin. *J. Neurosci.* 32 (1), 183–193.
- Wang, C.E., Tydlacka, S., Orr, A.L., Yang, S.H., Graham, R.K., Hayden, M.R., et al., 2008. Accumulation of N-terminal mutant huntingtin in mouse and monkey models implicated as a pathogenic mechanism in Huntington's disease. *Hum. Mol. Genet.* 17 (17), 2738–2751.
- Wang, S., Ke, S., Wu, Y., Zhang, D., Liu, B., He, Y.-H., et al., 2021. Functional Network of the Long Non-coding RNA Growth Arrest-Specific Transcript 5 and Its Interacting Proteins in Senescence, p. 12.

- Weinzimer, S.A., Gibson, T.B., Collett-Solberg, P.F., Khare, A., Liu, B., Cohen, P., 2001. Transferrin is an insulin-like growth factor-binding Protein-3 binding Protein1. *J. Clin. Endocrinol. Metabol.* 86 (4), 1806–1813.
- Wellington, C.L., Ellerby, L.M., Gutekunst, C.A., Rogers, D., Warby, S., Graham, R.K., et al., 2002. Caspase cleavage of mutant huntingtin precedes neurodegeneration in Huntington's disease. *J. Neurosci.* 22 (18), 7862–7872.
- Wilton, D.K., Stevens, B., 2020. The contribution of glial cells to Huntington's disease pathogenesis. *Neurobiol. Dis.* 143, 104963.
- Wong, B.K.Y., Ehrnhoefer, D.E., Graham, R.K., Martin, D.D.O., Ladha, S., Uribe, V., et al., 2015. Partial rescue of some features of Huntington disease in the genetic absence of caspase-6 in YAC128 mice. *Neurobiol. Dis.* 76, 24–36.
- Xu, J., Zhou, H., Xiang, G., 2022. Identification of Key Biomarkers and Pathways for Maintaining Cognitively Normal Brain Aging Based on Integrated Bioinformatics Analysis, 14.
- Yin, Y., Zhang, X., Williams, R., Wu, X., Anderson, D.D., Sonka, M., 2010. LOGISMOS—layered optimal graph image segmentation of multiple objects and surfaces: cartilage segmentation in the knee joint. *IEEE Trans. Med. Imaging* 29 (12), 2023–2037.
- Zeitlin, S., Liu, J.P., Chapman, D.L., Papaioannou, V.E., Efstratiadis, A., 1995. Increased apoptosis and early embryonic lethality in mice nullizygous for the Huntington's disease gene homologue. *Nat. Genet.* 11 (2), 155–163.
- Zhao, R.-b., Zhu, L.-h., Shu, J.-P., Qiao, L.-X., Xia, Z.-K., 2018. GAS5 silencing protects against hypoxia/ischemia-induced neonatal brain injury. *Biochem. Biophys. Res. Commun.* 497 (1), 285–291.
- Zhao, S., Devega, R., Francois, A., Kidane, D., 2021. Human ALKBH6 is required for maintenance of genomic stability and promoting cell survival during exposure of alkylating agents in pancreatic Cancer. *Front. Genet.* 12, 635808.
- Zhou, L., Shao, C.Y., Xie, Y.J., Wang, N., Xu, S.M., Luo, B.Y., et al., 2020. Gab1 mediates PDGF signaling and is essential to oligodendrocyte differentiation and CNS myelination. *eLife.* 9.
- Ziabska, K., Ziemka-Nalecz, M., Pawelec, P., Sypecka, J., Zalewska, T., 2021. Aberrant Complement System Activation in Neurological Disorders. 22 (9), 4675.